J. Fluid Mech. (2007), *vol.* 578, *pp.* 119–138.
doi:10.1017/S0022112007004892 Printed in the United Kingdom

The role of viscosity and surface tension in bubble entrapment during drop impact onto a deep liquid pool

Q. DENG, A. V. ANILKUMAR† AND T. G. WANG

Department of Mechanical Engineering, Vanderbilt University Nashville, TN-37235, USA

(Received 30 November 2005 and in revised form 12 November 2006)

The phenomenon of liquid drop impact onto the surface of a deep pool of the same liquid is studied in the context of bubble entrapment, using high-resolution digital photography. Three liquids, pure water, glycerin/water mixtures, and silicon oil, have been used to investigate the effect of viscosity (μ) and surface tension (σ) on regular bubble entrapment, and the associated impact crater signatures. The global viscous effect is seen as a shift in the classical inviscid bubble entrapment limits, whereas, at the impact crater, the local effect is seen as a weakening of the capillary wave, which is responsible for bubble pinching, and a weakening of the intensity of crater rebound. Bubble entrapment, which results from a competition between concentric capillary pinching of the crater cusp and viscous damping, is captured well by the capillary number Ca ($Ca = \mu V_i/\sigma$, where V_i is the drop impact velocity). The measured peak entrapped bubble size decreases exponentially as capillary number increases, with the cut-off capillary number for bubble entrapment estimated to be around 0.6. The critical crater cone angle for peak bubble pinch-off weakly increases with capillary number, with the measured value in agreement with theory in the inviscid limit (low Ca). Additionally, the growth of the main body of the high-speed thin jet, formed immediately following bubble pinch-off, is fitted to a power-law singularity model. This suggests that the thin jet is similar to the hydraulic jets produced by the collapse of free-surface standing waves.

1. Introduction

The phenomenon of drop impact onto a pool of the same liquid, a very familiar scene observed during a rainfall, has been studied for nearly a century. While initial studies were motivated purely by scientific curiosity, the more recent studies have been prompted by the practical application of this phenomenon. For example, the vortex ring developed after low-energy drop impact can enhance the mixing of drop fluid with pool fluid (Anilkumar, Lee & Wang 1991). The underwater noise generated during raindrop impact is caused by the oscillation of small air bubbles, repeatedly entrapped at the bottom of the impact crater under certain conditions (Oguz & Prosperetti 1991; Prosperetti & Oguz 1993). Air entrapment increases gas transport between the atmosphere and the ocean, and also provides boiling nucleation sites for the bulk fluid (Thoroddsen, Etoh & Takehara 2003).

† Author to whom correspondence should be addressed

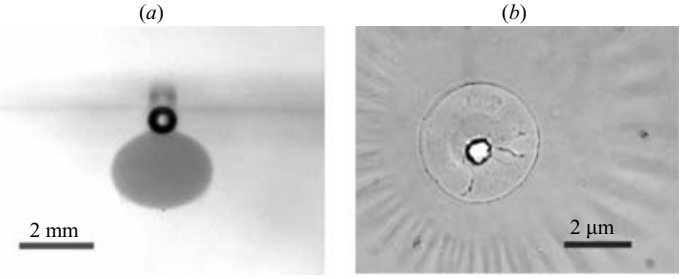

FIGURE 1. Bubble entrapment observed during the encapsulation process: (*a*) an entrapped air bubble is embedded on the drop/capsule surface, impeding chemical reaction locally; (*b*) an enlarged picture showing surface defects due to the presence, and eventual rupture, of the air bubble.

Recently, it has been noted in our laboratory that entrapped air bubbles following drop impact pose a new problem in the cell encapsulation process, where hormone-secreting cells are encapsulated in polymer-membrane-based capsules (Wang *et al.* 1997). These capsules are made by continuously dispensing viscous poly-anion drops into a water-like poly-cation solution (Anilkumar, Lacik & Wang 2001), where the membrane-forming chemical reaction proceeds as the drop contacts the reactive bulk during impact. At that time, a single air bubble is often embedded on the drop surface, locally impeding the chemical reaction and membrane formation, as seen in figure 1(*a*). The presence of such an air bubble adversely affects the capsule surface quality and makes the capsule vulnerable to immune attack (figure 1*b*). This problem has stimulated our current study of drop impact. As a first step to a complete understanding of the viscous reactive drop impact problem, here we examine the impact of a non-reactive viscous liquid drop onto the pool of the same liquid.

The physical forces involved in drop impact are surface tension, gravity, inertia and viscous damping. The viscous effect has been neglected in most previous works, but it will be a major focus of this paper. The dimensionless parameters involved in the inviscid drop impact problem are the Weber number *We* and the Froude number *Fr*. *We* is the ratio of the kinetic energy to the surface energy, and *Fr* is the ratio of the kinetic energy to the gravitational potential energy. In the context of liquid drop impact, they can be expressed as

$$We = \rho D V_i^2/\sigma, \quad Fr = V_i^2/(gD). \tag{1}$$

Here V_i is the impact velocity, D the drop diameter, σ the surface tension and ρ the density of the drop/pool liquid, and g the acceleration due to gravity.

In general, there are three types of patterns observed as the impacting drop kinetic energy increases, namely: (i) vortex ring, (ii) regular bubble entrapment and (iii) crown formation or splashing. In low-energy impact, which is also called coalescence in the literature, the drop surface energy becomes important. After initial contact of the drop with the bulk, the drop liquid evolves into a vortex ring structure, which quickly penetrates downward into the bulk, until viscosity dampens the kinetic energy associated with the vortex ring (Chapman & Critchlow 1967; Hsiao, Lichter & Quintero 1988; Anilkumar *et al.* 1991; Peck & Sigurdson 1994; Cresswell & Morton 1995; Dooley *et al.* 1997). As the impact energy is increased, vortex ring formation is suppressed. Then as Pumphrey & Elmore (1990) first reported, a single air bubble is entrapped at the bottom of the impact crater. They defined this event as regular bubble entrainment (entrapment) since the bubble pinch-off is reproducible.

They also experimentally determined the lower and upper limits for the regular bubble entrapment phenomenon, and scaled them as $We \sim Fr^{0.179}$ and $We \sim Fr^{0.248}$ respectively. In the regime above the regular bubble entrapment limit, the crater bottom reverses direction before it can pinch off an air bubble. Here, a thick rounded jet is observed rising from the crater centre and one or more drops break off from its tip (Rein 1996). At even higher impact kinetic energy, the edge of the crater wall ejects a sheet of liquid upward. The liquid sheet is unstable due to surface tension effects and ejects tiny droplets from its upper rim, forming the well-known crown pattern (Worthington 1908). A complete plot that delineates regimes, for each impact signature, in the *We–Fr* plane is provided by Leng (2001).

In the past two decades, many studies have focused on understanding the mechanism of regular bubble entrapment and the associated phenomena, such as conical flow around the crater and the high-rising thin jet. Oguz & Prosperetti (1990) stated that "whether a bubble is entrapped or not is determined by a delicate balance between the times at which the outward motion of the crater wall is reversed at different positions". Based on the observations of the experimental results of Pumphrey & Elmore (1990), they further proposed two scaling models showing that the lower and upper limits for bubble entrapment are $We \sim Fr^{1/5}$ and $We \sim Fr^{1/4}$ respectively, which agreed well with the experimental data. In their analysis, they did not mention the travelling capillary ripple along the crater wall, observed by Pumphrey & Elmore (1990). Later studies, however, have addressed the role of the travelling capillary wave in regular bubble entrapment (Longuet-Higgins 1990; Oguz & Prosperetti 1991; Morton, Rudman & Leng 2000; Elmore, Chahine & Oguz 2001).

It has been observed that the impact crater resembles an inverted cone shape prior to bubble entrapment. Longuet-Higgins (1983, 1990) first proposed a general velocity potential model, neglecting gravity and surface tension effects, leading to a solution with a hyperboloid free surface, which fairly well represents the conical crater shape before bubble pinch-off. More interestingly, he found that there exists a critical cone angle of 109.5°, at which the global flow field diverges. This critical cone angle compares well with the numerical results of Oguz & Prosperetti (1990) and the experimental results of Leng (2001); however, it is not clear why the bubble entrapment event occurs at this point.

Rein (1996) carried out a series of experiments using 2.3 mm water drops to investigate the transitional regime between coalescence and splashing. He pointed out that drop impact in the region of regular bubble entrapment is always accompanied by the ejection of a high-rising thin liquid jet originating from the centre of the impact crater. He attributed this phenomenon to the occurrence of a high-pressure stagnation region during crater collapse. More recent studies have shown high-speed thin jet formation in other hydrodynamic situations like surface wave collapse (Hogrefe *et al.* 1998; Zeff *et al.* 2002) and collapse of surface voids (Lohse *et al.* 2004; Bergmann *et al.* 2006). In these contexts, the jet formation is driven by the inertial focusing of the bulk flow during the collapse. To demonstrate this focusing effect, the surface geometries prior to collapse have been scaled as a power-law dependence with time (Leppinen & Lister 2003; Burton, Waldrep & Taborek 2005; Gordillo *et al.* 2005; Bergmann *et al.* 2006). A similar scaling approach in the drop impact problem could draw attention to the bulk flow focusing effects on bubble entrapment and thin jet formation.

Many of the earlier studies on drop impact onto a deep liquid pool have been carried out using pure water as the medium. Very few studies have investigated the effects of viscosity and surface tension, except the one by Pumphrey & Elmore

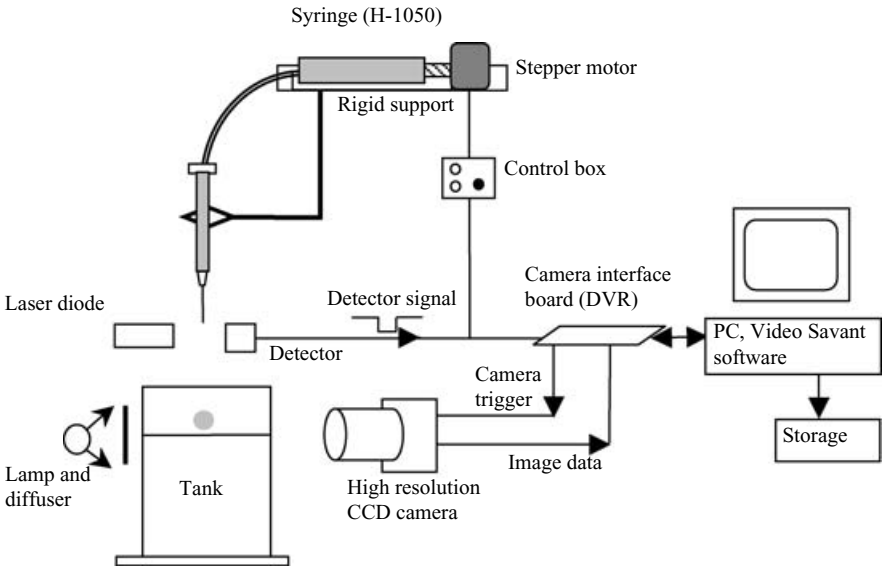

FIGURE 2. Schematic drawing of the experimental set-up.

(1990) who note that bubble entrapment is totally suppressed when a small amount of surfactant is added to the liquid. To further understand the bubble entrapment phenomenon, it is necessary to examine the role of viscosity and surface tension. In practice, impacting drops and bulk fluid may consist of different liquids for which the viscosity and surface tension may vary in a wide range. Three liquids, i.e. distilled water, silicon oil, and glycerin–water mixtures, have been used as experimental fluids, allowing for the variation of both surface tension and viscosity. A frame-on-demand photographic method has been used to obtain high spatial and temporal resolution images of the impact events. For each set of liquids, dynamic impact conditions for bubble entrapment have been measured and expressed in dimensionless Weber and Froude numbers. Critical crater shape, which represents the crater shape just before the bubble pinch-off, and entrapped air bubble size have been examined in detail. Another aspect of interest in this work is to quantify the high-rising thin jet profile following bubble entrapment. A power-law singularity with respect to time has been fitted from the experimental data.

2. Experimental method

Figure 2 is a schematic drawing of the experimental set-up. A square transparent Lucite tank of 7.6 cm side and 17.8 cm height is used to hold the bulk liquid. The container is filled to almost four-fifths of the way to the top. The drop liquid is loaded into a high-capacity syringe (Hamilton Gastight 1050), which is mounted horizontally in a screw-driven slide (Velmex) actuated by a low-speed stepper motor. A small luer-lock syringe (3 ml) with a needle termination is connected to the outlet of the high-capacity syringe through silicon rubber tubing. The needle is positioned vertically above the center of the liquid tank. A laser diode-detector combination is mounted below the needle so that each time a drop pinches off from the needle, the detector can detect it. The stepper motor can be switched on manually through a control box, and is automatically switched off once a pinched-off drop is detected. The pendant

	Density (10^3 kg m^{-3})	Surface tension (dyn cm^{-1})	Viscosity (cP)
*Distilled water	0.998	73.6	1
#1 cS silicon oil[$]	0.818	17.4	0.82
#2 cS silicon oil[$]	0.878	18.9	1.76
#5 cS silicon oil[$]	0.909	19.7	4.55
*50 wt% glycerin/water	1.126	69.2	5.9
*60 wt% glycerin/water	1.153	67.2	10.2
*67 wt% glycerin/water	1.172	63.9	14.7

TABLE 1. Properties of liquids used in the experiments (*measured data; #manufacturer's data). [$]Dow Corning 200 Series

drop grows very slowly at the tip of the needle and at a critical point when the drop weight exceeds the surface tension restraining force it pinches off. A digital CCD camera (UNIQ-2000-12B), in combination with a Micro Nikkor 200 mm lens, is used to record the interface deformations during drop impact. The camera resolution is 1680×1234 pixels, and the sharpest spatial resolution of this photographic system is 9.0 micron/pixel. A high-intensity fibre optic lamp in conjunction with a diffuser is used to uniformly illuminate the field of view. The typical frame exposure time is 50 μs.

The diode-detector pair generates a timing TTL signal each time a drop pinches off from the tip and crosses the laser beam. Besides switching off the stepper motor, this signal is also sent to the camera interface board (DVR-Express, I/O industries Inc.) and suitably delayed before triggering the camera's electrical shutter. The control of the delay time is achieved through the image acquiring software (Video Savant 4.0, I/O Industries Inc.). The delay period can be programmed in units of 25 ns. For each run, a single frame was recorded and labelled with a time stamp of the delay period. By changing the delay time and repeating the same impact experiment, a sequence of frames with both high spatial and temporal resolution was generated. The frame-on-demand photographic system requires a very high repeatability of the drop size, and a high accuracy of the drop detecting signal. In order to improve the drop size repeatability, the needle tip was ground flat and a teflon (hydrophobic) coating was applied on the needle outer wall. The growing time for each drop before detachment is approximately one minute, which ensures that the internal flow disturbances during the drop growth are small. The timing uncertainty of the entire system has been evaluated to be about 0.08 ms.

Three sets of liquids have been used in this study: distilled water, glycerin/water mixtures and silicon oil (Dow Corning 200 Series Fluid). The properties of silicon oil are available through the manufacturer's data sheet. Different concentrations of glycerin/water mixtures were made by mixing distilled water and pure glycerin (Fisher Scientific) in appropriate weight ratios. The viscosities of these mixtures were measured by a falling-ball-type viscometer. The surface tension was measured through a ring-type tensiometer (Fisher Surface Tensionmat, Model 21). Table 1 lists the properties of the liquids used in this study. In some cases, a small amount (less than 0.5% in weight) of dye was added to the drop liquid in order to highlight the drop liquid during impact. The dye added to silicon oil was oil orange powder (DuPont), and red food colour (McCormick) was used for glycerin/water mixtures. The addition of dye to the test fluids had negligible effects on their physical properties.

Drop size, bubble size, crater cone angle and other geometrical parameters were measured directly from digital images (in bit-map format) through *Paint* tool in Windows XP. The impacting drop size depends on liquid density, surface tension and the outer diameter of the needle. In our experiments, 30G, 26G and 18G needles were used, with their outer diameters measured as 0.30 mm, 0.41 mm and 1.26 mm respectively. This gave drop sizes in the range 1.50 mm to 3.29 mm. The variation of the drop size between different runs, for the same size needle, was evaluated to be less than 1%. This was ascertained by impacting a set of (about five) water drops onto a deep pool of oil and photographing the slowly moving and non-oscillating drops. This method virtually assures an undistorted drop image, which was suitable for drop size calibration.

Owing to the disturbances originating during drop pinch-off, the drop oscillates and thereby its impact shape is non-spherical. These oscillations are weakened by drop viscosity, and this effect is stronger for smaller drops. The oscillations themselves, however, occur over an equilibrium spherical shape, which is unaffected by the aerodynamic drag, owing to the short fall heights (Andsager, Beard & Laird 1999). In the context of a water drop impact, the measured skew factor, which denotes the relative difference ΔR between two half-axes of an ellipsoid scaled by drop radius, reaches maximum of about 3%, while in most other cases the shape deviation is much lower. It is assumed that such low oscillation amplitudes will not affect the entrapment phenomenon. However, in the vortex ring regime, the vortex penetration has been observed to be influenced by the oscillation state of the impacting drop (Rodriguez & Mesler 1988; Durst 1996).

The impact velocity was regulated by changing the falling height of the impacting drop, which is the distance from the tip of the needle to the surface of the liquid pool. The actual impact velocity was measured by multi-exposure method, with the aid of a stroboscope (GenRad 1539A). The measured horizontal velocity at the impact position was less than 0.5% of the vertical velocity, which indicates that all drops impact relatively normally onto the surface. If the falling height is too long, even the small horizontal disturbance will change the position of impact, moving the impact crater out of the field of view. With these concerns, the impact velocity range was chosen between 0.9 and 3.3 m s^{-1}. This experimental range guaranteed that the experiments encompassed the regular bubble entrapment regime. Based on the measurements described above, the computed *We* and *Fr* have been estimated to have errors of less than 3%. An edge-detecting program was developed to extract accurate profiles of the main body of the high-rising thin jet, and the data sets together with time information of each frame were further processed through *Polymath* software.

3. Results

3.1. *Preliminary experiments: low-viscosity drop impact*

The main objective of the preliminary experiments with low-viscosity drop liquid (1 cS) was to corroborate the baseline results available in the literature, before examining the effects of fluid properties on bubble entrapment. A secondary objective was to work with silicon oil, in addition to water-based systems, as it is a well-characterized liquid, is readily available in various viscosity grades, and its surface tension is almost a quarter of that of water. Further, unlike water, the surface tension of silicon oil is insensitive to minor contamination, if any, and the working liquid does not require mixing, and can be stored in the syringe over a long time.

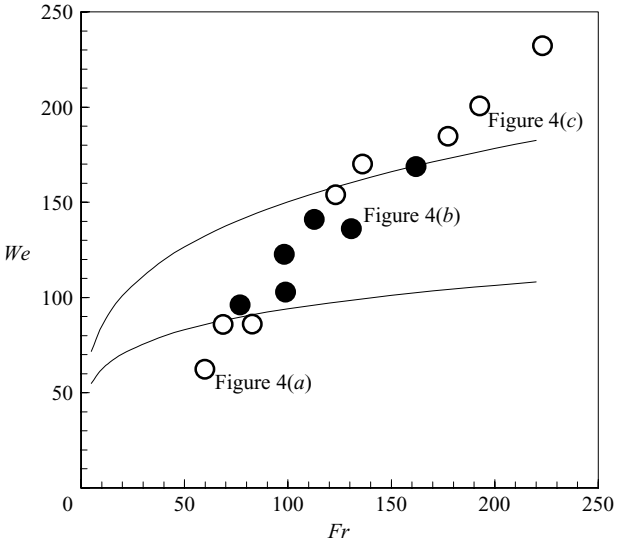

FIGURE 3. *We–Fr* plot showing the regular bubble entrapment regime for a low-viscosity liquid system. Solid lines are regular entrapment limits determined for a water impact system by Pumphrey & Elmore (1990). Filled circles denote regular bubble entrapment, and open circles denote absence of regular bubble entrapment, for low-viscosity (0.82 cP) oil drop impact, from our experiments.

The experiments with the low-viscosity silicon oil were carried out using two different needles and with the drop impact velocity in the range of 0.90 to 1.69 m s^{-1}. For each run, the impact condition was plotted as a data point in the *We–Fr* plane, with appropriate symbols to denote the observed entrapment signature. As shown in figure 3, regular entrapment occurs within a limited parameter regime, which is close to that established by Pumphrey & Elmore (1990) using the water system. The latter regime has also been corroborated by our water-based experiments (data not shown).

The crater profiles, within and outside the regular entrapment regime, for 1cS oil drop impact are shown in figure 4. Figure 4(*a*) shows the crater profiles for impact parameters below the entrapment regime (refer to the corresponding data point in figure 3). The thick dark horizontal line at the top in each picture represents the oil–air interface. The evolving dark feature is the impact crater. The dyed drop fluid can be seen as a grey area around the crater bottom. Since the drop fluid and the pool fluid are identical, the drop fluid would be invisible, unless dyed. The drop fluid is flattened immediately after initial contact, followed by the growth of the impact crater. The drop fluid expands as the crater grows, then forms a circular blob near the crater sidewall. When the crater starts to recede, the drop fluid aggregates at the crater bottom, and organizes into a vortex ring structure. At later time, the ring moves downward, with a filament extended to the free surface. A pair of small air bubbles, about 0.05 mm in size, are seen at the bottom of the drop fluid (vortex ring). These air bubbles are caused by the sudden rupture and contraction of the air film, located between the drop and the bulk interface, and they are not formed by the regular entrapment process (Thoroddsen *et al.* 2003).

As the impact velocity is increased, so that the impact parameters (*We* and *Fr*) are in the regular entrapment regime (figure 3), a different crater evolution is seen. After the crater grows to its maximum depth, its bottom stays at the same position

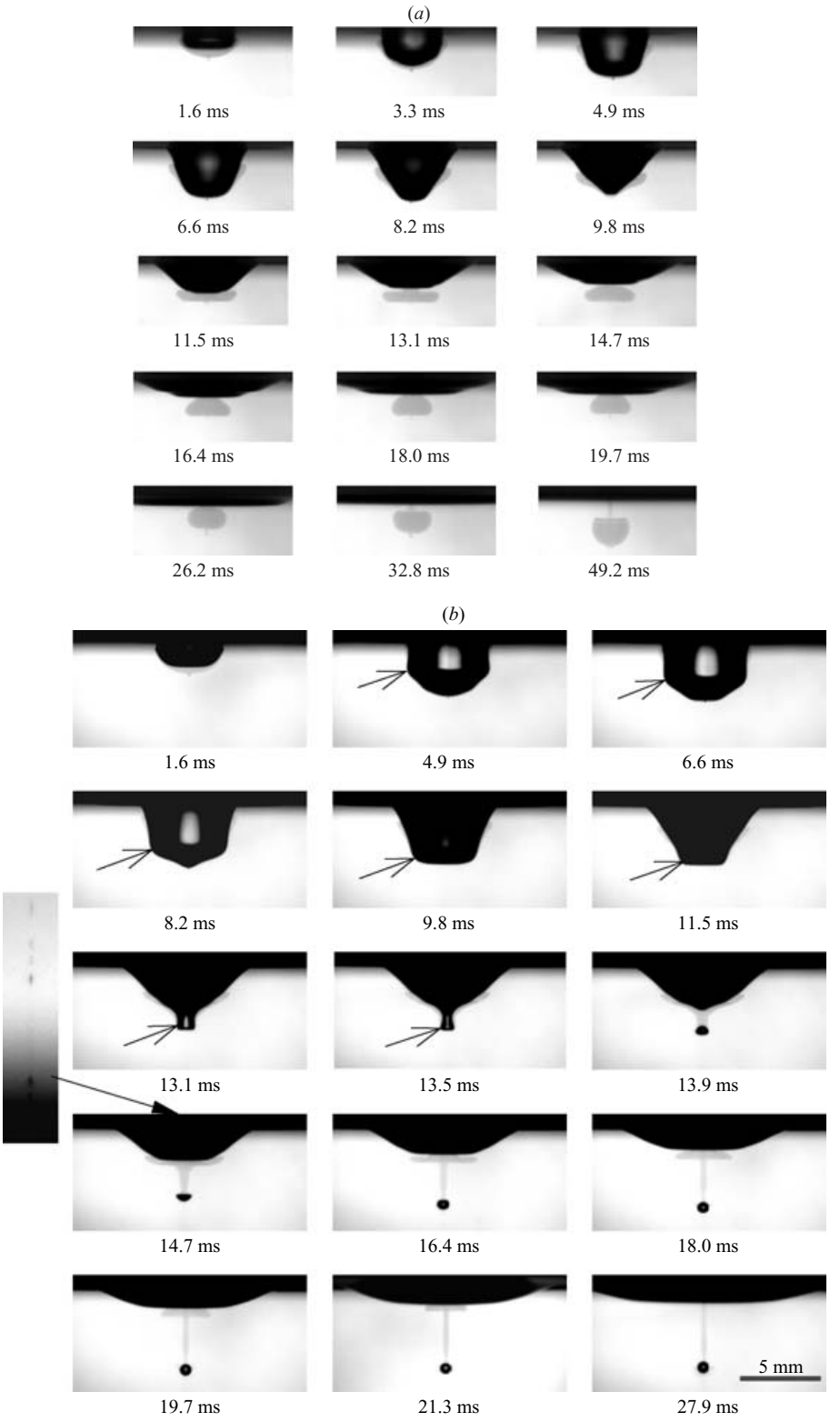

FIGURE 4(*a*, *b*). For caption see facing page.

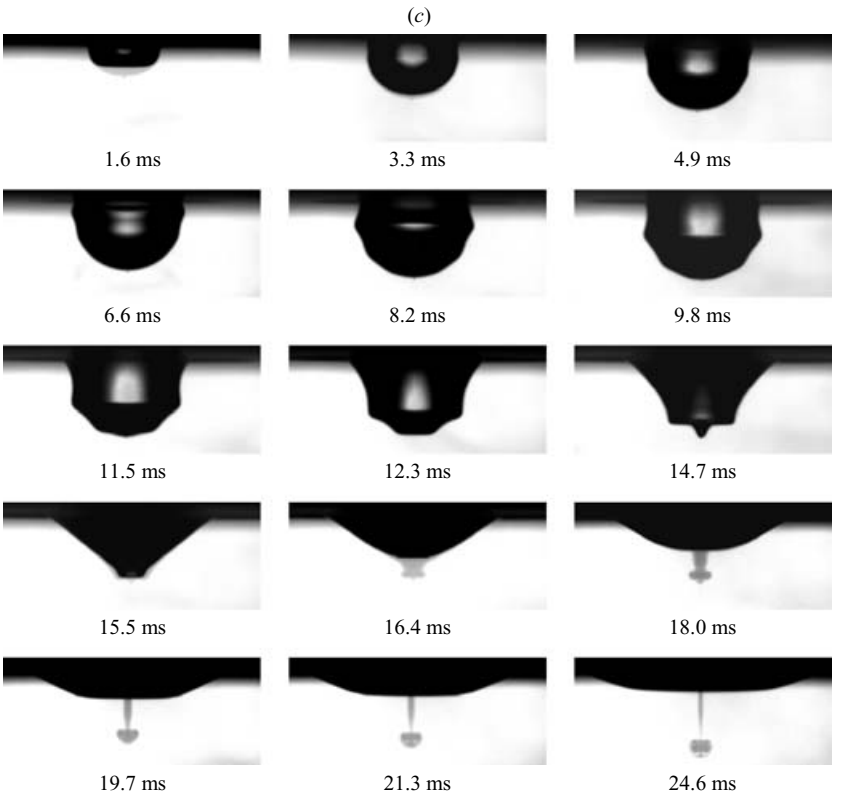

FIGURE 4. Pictures showing crater profile evolution for low-viscosity oil drop (0.82 cP) impact onto a deep pool of the same liquid, with the impact parameters (*We, Fr*) located (*a*) below, (*b*) within, and (*c*) above the regular bubble entrapment regime. Sequences (*a*), (*b*), (*c*) relate to corresponding data points in figure 3. The experiments have been conducted with 1.5 mm drops, and the impact Reynolds numbers *Re* for the three cases are 1409, 2004, and 2434 respectively.

for a while and the sidewall starts to converge, transforming the crater shape from hemispherical to a conical. At the same time, a concentric capillary ripple travels along the crater sidewall, as shown by the arrows indicating the wave troughs in figure 4(*b*). The origin of this traveling capillary wave is related to the strong surface disturbance following initial contact of the impacting drop (Oguz & Prosperetti 1991; Weiss & Yarin 1999; Morton *et al.* 2000; Mohamed-Kassim & Longmire 2004). While some of the concentric ripples emanate away from the impact crater rim, others travel along the crater wall towards the symmetry axis. If a capillary wave reaches the bottom of the crater at the right time its crest closes concentrically to trap an air bubble. After bubble pinch-off, a very high-speed thin jet is ejected upward, as seen by the column of droplets in the inset ($t = 14.7$ ms, figure 4*b*). The jet starts to thicken as the crater bottom begins to rebound. The thin grey filament from the bubble to the crater indicates that most of the drop fluid moves upward along with the bulk reverse flow.

Figure 4(*c*) shows the evolving crater signatures on further increasing the impact velocity, whereby the impact parameters are above the entrapment regime (figure 3). The early development of the crater profile resembles a growing hemisphere. The drop fluid is hardly seen in the pictures since it is evenly distributed along the crater

and forms a thin film. In contrast to the bubble entrapment craters of figure 4(*b*), where a single concentric capillary ripple is involved, the crater inner surface here is disturbed by a series of concentric ripples. This changes the morphology of the crater and interferes with the effective closure of the crater wall as seen in the earlier scenario (figure 4*b*). There is no dramatic crater closure and appearance of a thin jet; instead the crater rebound is through a thick jet. Since the impact parameters for figure 4(*c*) are still close to the upper entrapment boundary, a vestigial capillary closure and entrapment effect can be seen in the time frame corresponding to 14.7 ms.

An unexpected observation in figure 4(*c*) is that a vortex ring forms again at the condition above the upper limit for bubble entrapment. After $t = 15.5$ ms, the distributed drop fluid starts to concentrate again at the crater bottom and develops into a small vortex ring structure. The ring grows slowly and moves downward, leaving a filament behind. This vortex ring formation above the regular entrapment limit has not been observed experimentally in the water system. However, numerical simulations of Morton *et al.* (2000) predict vortex ring formation both below and above the regular entrapment limits. They state that at higher energy impact, vorticity is generated in the vicinity of the traveling capillary wave, whereas in the traditional low-*We* vortex ring regime, vorticity is generated due to the initial contact between drop liquid and the bulk. This seems to agree with our observations with the oil system (figure 4*c*). The vortex ring structure can only be seen if the vorticity can concentrate in a certain area. If the local convective flow is strong, vortex ring formation is affected. This is probably the reason why no vortex ring is observed in regular bubble entrapment, where the bulk flow convective effects are strong.

3.2. *Viscous drop impact*

Our study with low-viscosity liquid systems has established the importance of the timing of capillary wave arrival in trapping of the bubble. In this section, we examine the role of viscosity in bubble entrapment, in particular the effect of viscosity on the capillary wave and on the crater rebound dynamics. Glycerin/water (G/W) mixtures of various viscosities have been used to investigate the viscous effect on regular bubble entrapment during drop impact.

The limits a–a', b–b', c–c' in figure 5(*b*) represent the entrapment boundaries for the 1 cP, 5.9 cP and 10.2 cP glycerin/water systems respectively. As a general rule, the impact energy requirements for bubble entrapment are higher as the viscosity increases. The detailed crater morphology at the critical moment when the crater tip rebounds is shown in figure 5(*a*) through the picture series A, B, C, with the subscripts '0' representing below, '1' representing inside, and '2' representing above the respective bubble entrapment regimes. The picture series D corresponds to the system with 14.7 cP viscosity, where no bubble entrapment is observed.

From the first group of pictures A_0, B_0, C_0 (figure 5*a*), which represent impact conditions below the respective regular entrapment limits, the effect of viscosity can clearly be noticed as a damping effect on the amplitude of the traveling capillary wave. From the next group A_1, B_1, C_1 which represent impact conditions within the respective entrapment limits, it is observed that the size of the entrapped bubble decreases as viscosity increases, to the point where there is no entrapment at the highest viscosity of 14.7 cP (picture D_1). The third picture series A_2, B_2, C_2 which represent conditions above the respective entrapment limits, shows the crater dynamics in competition with the capillary pinching. Clearly, in A_2, the low-viscosity case, the crater bottom has reversed direction, before capillary crest arrival, thereby preventing bubble entrapment. A similar effect is seen as the viscosity is increased to 5.9 cP, where

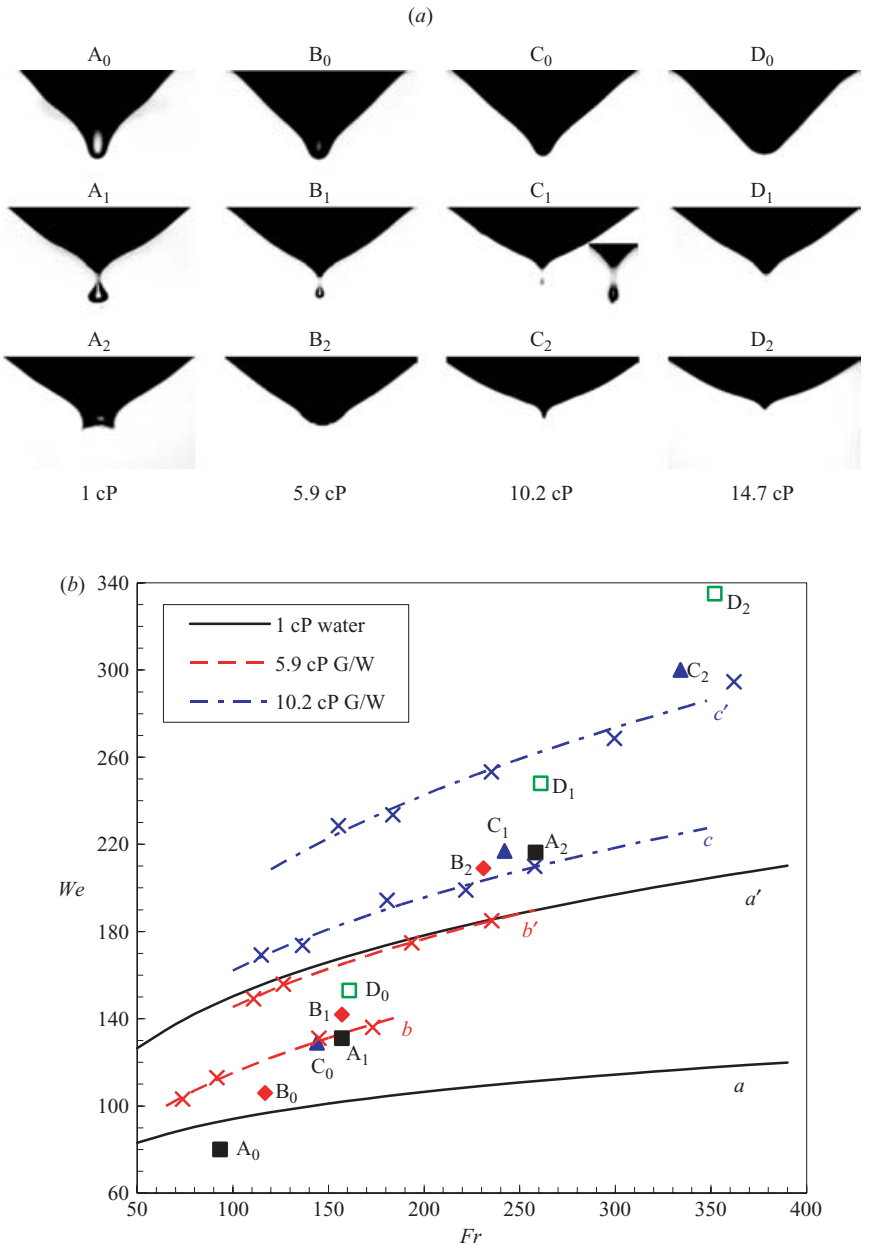

FIGURE 5. Comparison of the critical crater shapes and entrapment regimes for test liquids with different viscosities using the glycerin/water system: (*a*) critical crater shapes corresponding to specific locations in (*b*); subscript '0' represents below, '1' within and '2' above the corresponding entrapment regimes; (*b*) entrapment regimes *a*–*a*′, *b*–*b*′, *c*–*c*′ for systems with viscosities 1 cP, 5.9 cP and 10.2 cP respectively.

the crater is in reversal before capillary pinch-off. However, here, the crater base is rounder and the rebound process is weaker. As the viscosity is further increased, the effect of viscous damping both on the intensity of capillary wave and on the intensity of crater cusp reversal is stronger, complicating, yet preventing, the entrapment process.

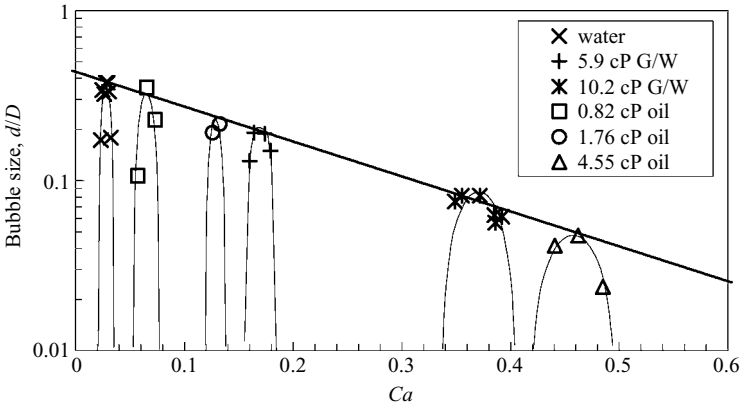

FIGURE 6. Variation of entrapped bubble size, for different drop impact conditions, as a function of the capillary number *Ca*.

4. Analysis and discussion

4.1. *Role of viscosity*

The global role of viscosity is seen as a change in the lower and upper regular entrapment limits, as shown in figure 5(*b*). In general, the impact energy requirement for bubble entrapment is increased with viscosity. The entrapment limits represent the subtlety of the timing in the bubble entrapment scenario: the capillary crest has to be at the right place at the right time, i.e. before crater reversal. If the sole effect of viscosity is to dampen the capillary ripple, then the entrapment limits should shrink. This appears to be the predominant effect, as seen for the 5.9 cP case. However, viscosity also weakens the crater cusp reversal mechanism, to the point where it is no longer in competition with capillary pinching. This effect broadens the entrapment regime again, as seen for the 10.2 cP system. In other words, the viscous effect can be interpreted as a weakening of the capillary wave, and a weakening of the crater reversal dynamics. The size of the entrapped bubble, however, progressively decreases with viscosity as seen in the A_1, B_1, C_1 picture series of figure 5(*a*). For a viscosity of 14.7 cP, there is no bubble entrapment and the crater reversal process is weakened, resulting in the formation of a thick jet during rebound.

In general, viscosity affects the intensity of both the capillary ripple, responsible for bubble entrapment, and the crater cusp curvature. This indicates that when viscosity plays a role in drop impact, the *We–Fr* combination alone is not sufficient to describe the bubble entrapment phenomenon. In this case, there is a need for an additional dimensionless number that captures the interaction between the capillary ripple and the viscous damping effects.

It is suggested that the dimensionless capillary number

$$Ca = \frac{\mu V_i}{\sigma} \tag{2}$$

can capture this interactive effect.

Figure 6 shows the change in entrapped bubble size with capillary number. The diameters of entrapped bubbles were measured directly from the digital pictures. Bubbles that pinched off from the crater tip and were repeatable in occurrence were considered as regularly entrapped bubbles in our experiments. Only bubbles greater

than 4 pixels (about 0.04 mm) in size were used in our studies, owing to the limitations in optical resolution.

It is noted that the entrapped bubble size varies between the lower and the upper entrapment limits with a peak in the middle; the peak progressively getts less sharp with increasing Ca. The results show that the peak bubble size decreases from about 0.98 mm to about 0.19 mm as viscosity increases from 1 cP to 10.2 cP in the glycerin/water system, with the corresponding capillary number varying from $Ca = 0.04$ to $Ca = 0.37$. Experiments with a 14.7 cP glycerin/water mixture (67% weight percent) show no bubble entrapment in the Weber number regime from 98 to 452. Figure 6 also includes bubble entrapment data for silicon oil drops, with different viscosities, showing that the capillary number is suitable to characterize the bubble entrapment phenomenon.

When viscosity is involved in free-surface flow, it sets up a viscous stress that opposes the capillary pressure, the latter being proportional to the curvature of the interface. From figure 5(a) (A_1, B_1, C_1) we see that the entrapped bubble size is related to the curvature of the crater tip, just before pinch off. As Ca increases, the viscous effect dominates, and the capillary curvature at the cone tip must increase to balance the increased viscous stress on the free surface, and thereby the entrapped bubble size decreases. This trend is clearly shown in figure 6, which also indicates that the cut-off Ca value for bubble entrapment is around 0.6. Jeong & Moffatt (1992) studied the cusp formed between two counter-rotating cylinders below a free surface at low Reynolds number (Re). Their analytical solution suggests that the tip radius of curvature on the line of symmetry decreases as $\exp(-32\pi Ca)$. In the present context, it is reasonable to equate the radius of curvature at the crater tip to the entrapped bubble size, when bubble entrapment occurs. Although the current external flow field is different from Jeong & Moffatt's (1992) two-dimensional rotating-cylinder case, the measured peak entrapped bubble sizes fit well onto an exponential line with Ca, as seen by the data in figure 6. In our three-dimensional problem, the prefactor of Ca, which is 4.7, is much smaller than the about 100 from Jeong & Moffatt's solution for the two-dimensional case.

The viscous effect during the drop impact process can also be examined from an energy standpoint. Generally, there are two effects that need to be considered in this situation. The first is the viscous dissipation in the bulk during crater growth and rebound. The second is the viscous damping of the traveling capillary wave along the crater wall.

We first estimate the energy dissipated due to viscosity during the crater growth phase. The viscous dissipation energy, W_d, associated with the drop impact crater is given by Engel (1967) as

$$W_d = 8\pi\mu \int_0^t R \left(\frac{\mathrm{d}R}{\mathrm{d}t}\right)^2 \mathrm{d}t \tag{3}$$

where μ is the dynamic viscosity and R is the crater depth as a function of time t. Equation (3) assumes that the crater grows hemispherically, which is close to our observation. For a water drop 2.5 mm in diameter and impacting at 1.93 m s^{-1}, the viscous dissipation energy during the crater growth phase is approximately 1.4% of the original kinetic energy of the impacting drop. This indicates that the viscous damping effect on crater formation is negligible, for the low-viscosity drop impact system. In other words, the maximum crater depth is not affected by liquid viscosity in the low-viscosity range. In fact, when Pumphrey & Elmore (1990) and Leng (2001)

modelled the maximum crater depth by comparing energy transformed in the impact system, they neglected the viscous dissipation term, and yet got satisfying results.

The second effect of viscosity on drop impact can be to dampen the capillary wave energy and thereby weaken the entrapment process. If viscosity has significantly dampened the capillary wave before the crater grows to maximum depth, then bubble pinch-off should not happen. On the other hand, if the viscous effect on the capillary wave is not strong, then bubble entrapment may happen. Here, the viscous effect can be evaluated by the damping time constant τ. A requirement for bubble entrapment to occur can be expressed as

$$t_{c\max} < \tau \tag{4}$$

where $t_{c\max}$ is the crater growth time evaluated from drop–bulk initial contact to the moment when the crater reaches its maximum depth. Since crater growth is a process through which the kinetic energy from the impacting drop becomes potential energy stored in the crater, $t_{c\max}$ should be related to the impact kinetic energy. The viscous damping time constant τ for a capillary surface wave is (Lamb 1945)

$$\tau = \lambda^2/8\pi^2\nu \tag{5}$$

where λ is the capillary wavelength, and ν is the kinematic viscosity of the liquid. This expression is valid for all the liquid viscosities used in our experiments (Lamb 1945; Prosperetti 1976).

Using this equation to estimate the viscous effect on the traveling capillary wave, and taking $\lambda \sim D = 2.5$ mm, we obtain a viscous dissipation time constant $\tau = 79$ ms for the 2.5 mm water drop impact ($\nu = 1.0$ cS). From the present experiments, $t_{c\max}$ ranges from about 13 ms to 18 ms for all cases of a 2.5 mm water drop impact, within the regular entrapment regime. This suggests that viscous dissipation of the capillary wave is not dominant before bubble pinch-off in the low-viscosity water system. However, if the liquid is 67% glycerin/water mixture, the corresponding kinematic viscosity is increased to 12.6 times that of water, and the corresponding dissipation time constant τ becomes 6.3 ms. Since the overall crater formation process is affected negligibly by the viscosity increase, as the impact energy is proportionately increased, $t_{c\max}$ still remains within 13 ms to 18 ms. Thus, for the 12.6 cS glycerin/water case, τ is less than $t_{c\max}$, implying that viscosity will damp the capillary wave and thereby suppress bubble entrapment.

4.2. *Critical cone angle*

As reported in the literature, and confirmed by our experiments, the phenomenon of regular bubble entrapment is always associated with a conical crater shape and a high-rising thin jet. The gravitational-potential-induced crater shape recovery starts when the impact crater reaches its maximum depth (figure 4*b*). During the recovery, the sidewall slope decreases with time, indicating that there is a radial inward velocity component in the bulk flow which is progressively stronger at the crater bottom. From the picture series A_1, B_1, C_1 of figure 5(*a*), we see that the cone-shaped crater profiles take on an hour glass shape at the bottom, just before bubble pinch-off. This shape is a direct consequence of the timely arrival of the capillary ripple at the crater bottom, which sets up the conditions for bubble entrapment. The capillary crest facilitates the radial focusing of the bulk flow, leading to the dual events of bubble pinch-off and high-speed thin jet formation. In this sense, the focusing of the bulk flow, which follows the shape disturbance of the capillary ripple, appears to be different from pure inertial focusing as observed by Bergmann *et al.* (2006).

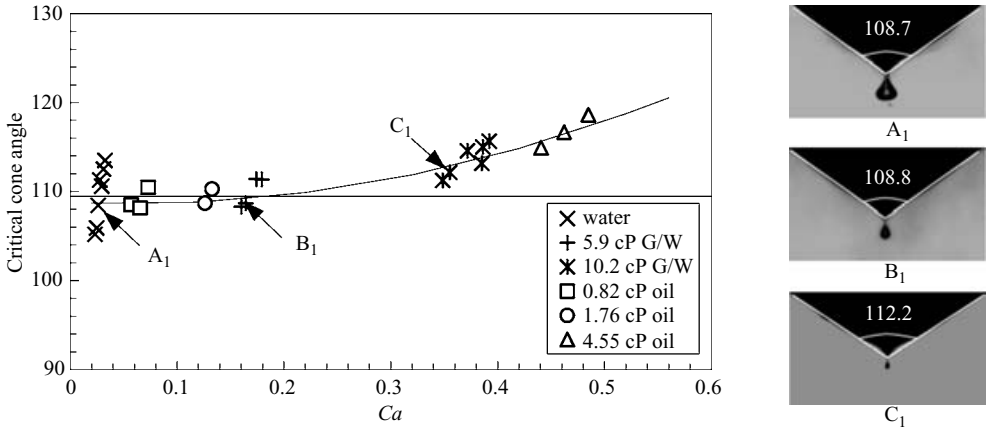

FIGURE 7. Variation of critical cone angle, measured at the moment of bubble pinch-off, as a function of the capillary number *Ca*. The solid line represents the critical cone angle prediction of Longuet-Higgins (1983). Data points A_1, B_1, C_1 correspond to the respective crater profiles of figure 5(*a*) (Pictures on the right show the critical cone angle measurement).

Longuet-Higgins' (1990) analytical model predicts that there is a critical cone angle associated with the so-called conical flow. He pointed out that when the crater cone reaches this critical cone angle, the entire velocity and acceleration fields tend to infinity as $t^{-1/3}$ and $t^{-4/3}$ respectively. This model does not include the surface tension term, so it cannot predict the bubble entrapment event as seen in the experiments. However, since the bulk flow diverges at the critical cone angle of 109.5°, the bubble pinch-off most probably occurs at this point.

In figure 7, the cone angles measured at the moment of bubble pinch-off, for different test liquids, have been plotted as a function of the capillary number. The critical cone angle has been determined by measuring the slopes of the straight lines connecting the pinch-off point to the cone base, as shown on the right of figure 7. The data spread for each liquid system represents the traverse from the lower entrapment limit to the upper entrapment limit, with the bubble size showing a peak in the middle. The dotted line connects the critical cone angle data, corresponding to peak bubble entrapment, for different liquid systems. The arrows represent the data points corresponding to pictures A_1, B_1, C_1 in figure 5(*a*). From figure 7, it is apparent that the critical cone angle for peak bubble entrapment varies weakly with the capillary number, and in the inviscid limit (low *Ca*) it agrees well with Longuet-Higgins' prediction.

4.3. *Power-law singularity of the thin jet*

Figure 8 shows the evolution of a high-rising thin jet, following bubble pinch-off, for a 5.9 cP glycerin/water drop impact. The labelled time for the individual pictures of figure 8 corresponds to the elapsed time following the moment of bubble pinch-off. In the first picture, the thin jet is visible above the crater rim, 1.1 ms after crater collapse. At that time the jet is very thin, and the Rayleigh capillary instability disintegrates the upper portion of the jet into minute droplets. The speed of the jet is so high that the droplet image is blurred despite a short exposure time of 50 μs. From this picture, it is estimated that the jet upward velocity is about $15\,\mathrm{m\,s^{-1}}$. As time elapses, the major part of the thin jet grows thicker and taller, and the upper portion develops a corrugated profile but does not pinch off into droplets. Later, as gravity effect

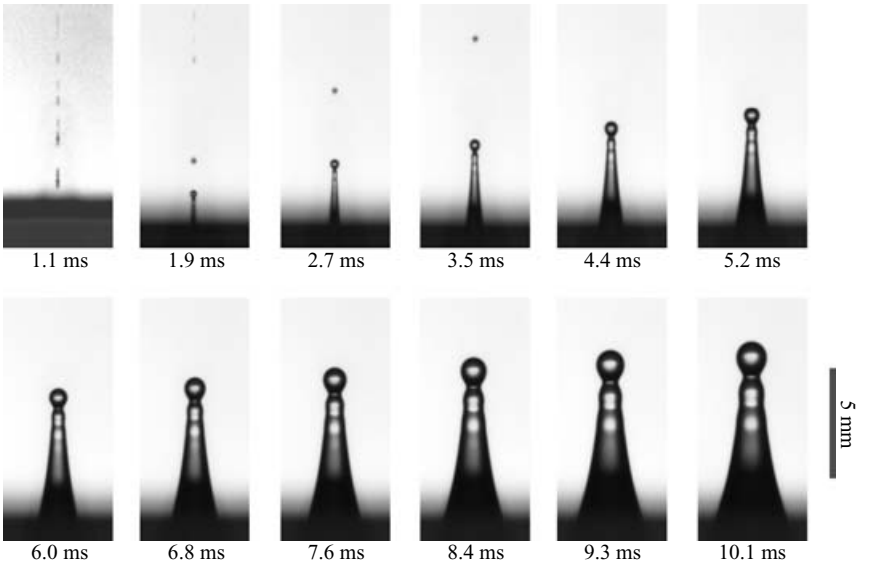

FIGURE 8. Pictures showing the high-speed thin jet and the main body of the reversed flow following bubble entrapment, during the impact of a 5.9 cP glycerin/water drop at $We = 117$, $Fr = 68$ (refer to figure 5*b*). Labels show the elapsed time following bubble pinch-off.

dominates, the jet stops growing in the vertical z-direction, and finally recedes to the equilibrium surface.

The high-speed thin jet is the consequence of the high-pressure stagnation resulting from the radial focusing of the bulk flow during bubble pinch-off. By characterizing the jet's growth profiles, using power-law scaling, one could potentially derive useful information about the dynamics of the bulk flow at the pinch-off moment. Here, we have analysed the jet profiles for the short time regime ($t < 10$ ms), where gravity has a very minimal role in the growth of the thin jet ($\frac{1}{2}gt^2/h \ll 1$; h is the height of the jet). Further, we have only examined the undistorted sidewall profile of the jet, and excluded the tip, which is strongly affected by capillary instability.

The construction of the fitting function for the jet profile has been motivated by the general solution form for the kinetic free-surface problem: $z = at^{\lambda}(rt^{\eta})^{\nu}$, derived by Hogrefe *et al.* (1998). Here z and r are the coordinates of a point located on the jet sidewall in a cylindrical coordinate system, originating at the bubble pinch-off point. The original frame analysis data (z, r, t) have been non-dimensionalized (z^*, r^*, t^*) by scaling z and r with D, and t with D/V_i. For convenience, we define our objective fitting function as

$$z^* = bt^{*\alpha}r^{*\beta}. \tag{6}$$

The nonlinear data regression has been done on *Polymath* software. If the fitting is good, then the data points of ($z^*/t^{*\alpha}$, r^*) should collapse onto one power-law curve of the form $z^*/t^{*\alpha} = br^{*\beta}$. This is shown by the main portion of figure 9. The inset in figure 9 represents the original r and z coordinates, obtained from the sequence of selected pictures shown in figure 8. The constants α and β in figure 9 are 0.656 and -0.435 for the 5.9 cP glycerin/water jet. The same fitting process has been implemented for data from water and 10.2 cP glycerin/water jets. The corresponding α and β values are 0.613 and -0.432 for the water jet, 0.686 and -0.540 for the

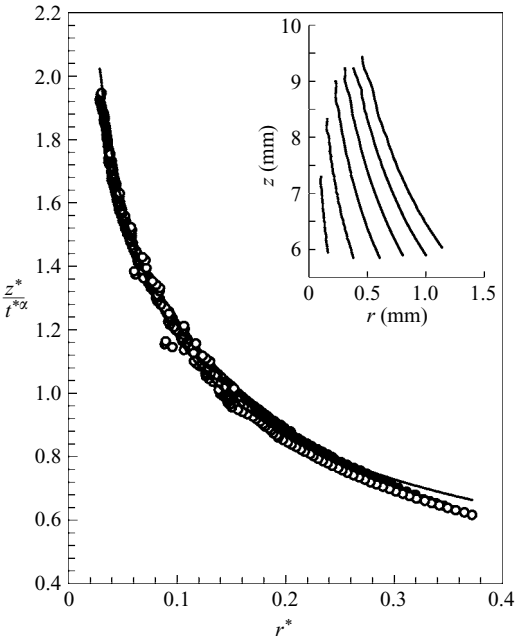

FIGURE 9. A sequence of jet profiles collapsing onto a power-law curve of the form: $z^*/t^{*\alpha} \sim r^{*\beta}$; for 5.9 cP glycerin/water jet $\alpha = 0.656$ and $\beta = -0.435$. The inset represents outlines of the jet extracted from pictures shown in figure 8, with the far left curve corresponding to $t = 2.7$ ms; the time interval between consecutive curves is 1.64 ± 0.04 ms.

10.2 cP glycerin/water jet. The jet analysis data do not show any strong effects of viscosity on α, for viscosities up to 10.2 cP.

According to equation (6), the vertical velocity and acceleration at the jet surface can be scaled as

$$\dot{z}^* \sim t^{*\alpha-1}, \quad \ddot{z}^* \sim t^{*\alpha-2}. \tag{7}$$

In the case of $\alpha = 0.656$, the velocity scales as $t^{*-0.344}$ and the acceleration scales as $t^{*-1.344}$. Consequently, at the time of origin, which is the pinch-off moment, both velocity and acceleration tend to approach infinity. This implies a singularity on the jet profile, as proved by the exceptionally high upward speed of the jet (figure 8, $t = 1.1$ ms). The degree of singularity can be evaluated by the α value. As α is positive and smaller than 1, at time very close to collapse ($t = 0+$), the velocity is higher for smaller α (equation (7)), which indicates a higher degree of singularity for the smaller α values.

The power-law scale of singularity for the jet profile has been reported for a wide range of free-surface flows, when the surface flow collapses at a certain point. It is valid for the hydraulic free-surface jets arising under conditions such as an overdriven standing wave (Hogrefe *et al.* 1998), cavity collapse inside a liquid body (Longuet-Higgins & Oguz 1995) and onset of an electrohydrodynamic spout (Oddershede & Nagel 2000), with the α values varying between 0.4 and 0.667 in these different situations. Figure 10 shows the temporal growth of the thin jet from the present experiments, with the slope of each data set representing the constant α. It appears that the experimental fitting constant α in each case is very close to the theoretical prediction of $\alpha = 2/3$ by Zeff *et al.* (2002).

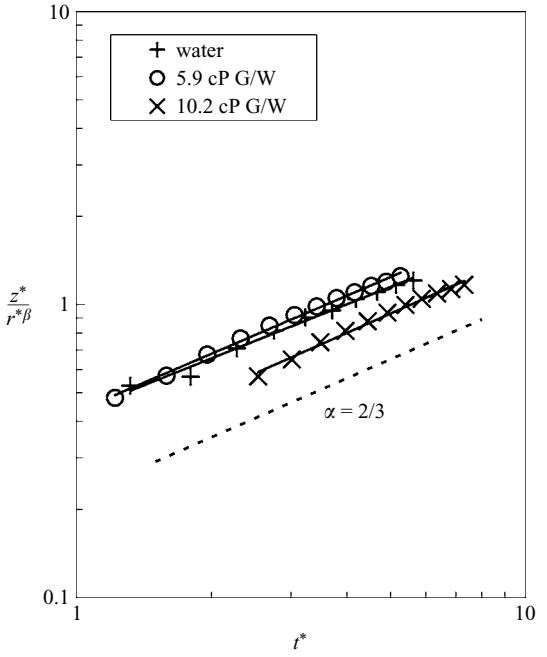

FIGURE 10. The temporal growth of the jet profiles for three different thin jets. The solid lines are the best-fit lines for each data set; the dotted line is a visual guide with the exponential constant $\alpha = 2/3$.

5. Conclusions

The role of viscosity and surface tension in bubble entrapment during drop impact onto a deep pool of the same liquid has been examined in detail, with different liquids. It is established that bubble entrapment results from an interplay between capillary wave pinching of the impact crater, and the viscous weakening of both the wave and the rebound of the crater bottom. Globally, the classical inviscid entrapment limits are shifted with viscosity, implying a stronger impact energy requirement for entrapment. Locally, the capillary wave crests are weakened by viscous damping so much that the peak entrapped bubble size progressively decreases with viscosity. Since the capillary wave is surface-tension based, and the damping is viscosity based, the effect is captured well by an additional dimensionless number, the capillary number. As the capillary number increases, the peak impact bubble size decreases exponentially, and for a capillary number greater than about 0.6 there is no bubble entrapment. The measured critical crater cone angle for peak bubble entrapment weakly increases with the capillary number and the measured value is in agreement with Longuet-Higgins' theory in the inviscid limit. The growth of the main body of the high-speed thin jet, formed immediately following bubble pinch-off, has been fitted to a power-law model and the temporal exponent, α, has been found to be smaller than 1. The thin jet is the result of the radial focusing of the bulk flow during bubble entrapment, and is of the same type of free-surface hydraulic jets as in surface wave collapse.

This research was supported by grants from the National Aeronautics and Space Administration (*Immunoisolation of Living Islets as a Functional Cure for Diabetes*), the Juvenile Diabetes Research Foundation (*Optimization Studies of PMCG Capsules*

towards a Functional Cure for Diabetes), the Evans-Gilruth Foundation, the Children's Miracle Foundation, and the Ronald McDonald Children's Charities. The authors wish to thank Ms Irena Trenary for her assistance in the experimental work.

REFERENCES

Andsager, K., Beard, K. V. & Laird, N. F. 1999 Laboratory measurements of axis ratios for large raindrops. *J. Atmos. Sci.* **56**, 2673–2683.

Anilkumar, A. V., Lacik, I. & Wang, T. G. 2001 A novel reactor for making uniform capsules. *Biotech. Bioengng* **75**, 581–589.

Anilkumar, A. V., Lee, C. P. & Wang, T. G. 1991 Surface-tension-induced mixing following coalescence of initially stationary drops. *Phys. Fluids* A **3**, 2587–2591.

Bergmann, R., Meer, D. V. D., Stijnaman, M., Sandtke, M., Posperetti, A. & Lohse, D. 2006 Giant bubble pinch-off. *Phys. Rev. Lett.* **96**, 154505.

Burton, J. C., Waldrep, R. & Taborek, P. 2005 Scaling and instabilities in bubble pinch-off. *Phys. Rev. Lett.* **94**, 184502.

Chapman, D. S. & Critchlow, P. R. 1967 Formation of vortex rings from falling drops. *J. Fluid Mech.* **29**, 177–185.

Cresswell, R. W. & Morton, B. R. 1995 Drop-formed vortex rings – the generation of vorticity. *Phys. Fluids* **7**, 1363–1369.

Dooley, B. S., Warncke, A. E., Gharib, M. & Tryggvason, G. 1997 Vortex ring generation due to the coalescence of a water drop at a free surface. *Exps. Fluids* **22**, 369–374.

Durst, F. 1996 Penetration length and diameter development of vortex rings generated by impacting water drops. *Exps. Fluids* **21**, 110–117.

Elmore, P. A., Chahine, G. L. & Oguz, H. N. 2001 Cavity and flow measurements of reproducible bubble entrainment following drop impacts. *Exps. Fluids* **31**, 664–673.

Engel, O. G. 1967 Initial pressure, initial flow velocity, and the time dependence of crater depth in fluid impacts. *J. Appl. Phys.* **38**, 3935–3940.

Gordillo, J. M., Sevilla, A., Rodriguez-Rodriguez, J. & Martinez-Bazan, C. 2005 Axisymmetric bubble pinch-off at high Reynolds numbers. *Phys. Rev. Lett.* **95**, 194501.

Hogrefe, J. E., Peffley, N. L., Goodridge, C. L., Shi, W. T., Hentschel, H. G. E. & Lathrop, D. P. 1998 Power-law singularities in gravity-capillary waves. *Physica D* **123**, 183–205.

Hsiao, M., Lichter, S. & Quintero, L. G. 1988 The critical Weber number for vortex and jet formation for drops impacting on a liquid pool. *Phys. Fluids*, **31**, 3560–3562.

Jeong, J. T. & Moffat, H. K. 1992 Free-surface cusps associated with flow at low Reynolds numbers. *J. Fluid Mech.* **241**, 1–22.

Lamb, H. 1945 *Hydrodynamics*. Dover.

Leng, L. J. 2001 Splash formation by spherical drops. *J. Fluid Mech.* **427**, 73–105.

Leppinen, D. & Lister, J. R. 2003 Capillary pinch-off in inviscid fluids. *Phys. Fluids*, **15**, 568–578.

Lohse, D., Bergmann, R., Mikkelsen, R., Zeilstra, C., Meer, D. V. D., Versluis, M., Weele, K. V. D., Hoef, M. V. D. & Kuipers, H. 2004 Impact on soft sand: void collapse and jet formation. *Phys. Rev. Lett.* **93**, 198003.

Longuet-Higgins, M. S. 1983 Bubbles, breaking waves and hyperbolic jets at a free surface. *J. Fluid Mech.* **127**, 103–121.

Longuet-Higgins, M. S. 1990 An analytic model of sound production by raindrops. *J. Fluid Mech.* **214**, 395–410.

Longuet-Higgins, M. S. & Oguz, H. 1995 Critical microjets in collapsing cavities. *J. Fluid Mech.* **290**, 183–201.

Mohamed-Kassim, Z. & Longmire, E. K. 2004 Drop coalescence through a liquid/liquid interface. *Phys. Fluids* **16**, 2170–2181.

Morton, D., Rudman, M. & Leng, L. J. 2000 An investigation of the flow regimes resulting from splashing drops. *Phys. Fluids* **12**, 747–763.

Oddershede, L. & Nagel, S. R. 2000 Singularity during the onset of an electrohydrodynamic spout. *Phys. Rev. Lett.* **85**, 1234–1237.

Oguz, H. N. & Prosperetti, A. 1990 Bubble entrainment by impact of drops on liquid surfaces. *J. Fluid Mech.* **219**, 143–179.

Oguz, H. N. & Prosperetti, A. 1991 Numerical calculations of the underwater noise of rain. *J. Fluid Mech.* **228**, 417–442.

Peck, B. & Sigurdson, L. 1994 The three-dimensional vortex structure of an impacting water drop. *Phys. Fluids* **6**, 564–576.

Prosperetti, A. 1976 Viscous effects on small-amplitude surface waves. *Phys. Fluids* **19**, 195–203.

Prosperetti, A. & Oguz, H. 1993 The impact of drops on liquid surfaces and the underwater noise of rain. *Annu. Rev. Fluid Mech.* **25**, 577–602.

Pumphrey, H. C. & Elmore, P. A. 1990 The entrainment of bubbles by drop impacts. *J. Fluid Mech.* **220**, 539–567.

Rein, M. 1996 The transitional regime between coalescing and splashing drops. *J. Fluid Mech.* **306**, 145–165.

Rodriguez, F. & Mesler, R. 1988 The penetration of drop-formed vortex rings into pools of liquid. *J. Colloid Interface Sci.* **121**, 121–129.

Thoroddsen, S. T., Etoh, T. G. & Takehara, K. 2003 Air entrapment under an impacting drop. *J. Fluid Mech.* **478**, 125–134.

Wang, T., Lacik, I., Brissova, M., Anilkumar, A. V., Prokop, A., Hunkeler, D., Green, R., Shahrokhi, K. & Powers, A. C. 1997 An encapsulation system for the immunoisolation of pancreatic islets. *Nature Biotechnol.* **15**, 358–362.

Weiss, D. A. & Yarin, A. L. 1999 Single drop impact onto liquid films: neck distortion, jetting, tiny bubble entrainment, and crown formation. *J. Fluid Mech.* **385**, 229–254.

Worthington, A. M. 1908 *A Study of Splash.* Longman's, Green and Company, London.

Zeff, B. W., Kleber, B., Fineberg, J. & Lathrop, D. P. 2002. Singularity dynamics in curvature collapse and jet eruption on a fluid surface. *Nature* **403**, 401–404.